PNAS RESEARCH ARTICLE | APPLIED PHYSICAL SCIENCES
BIOPHYSICS AND COMPUTATIONAL BIOLOGY

Geometric trade-off between contractile force and viscous drag determines the actomyosin-based motility of a cell-sized droplet

Ryota Sakamoto[a,1], Ziane Izri[b], Yuta Shimamoto[c], Makito Miyazaki[d,e,f,g], and Yusuke T. Maeda[a,1]

Edited by David Weitz, Harvard University, Cambridge, MA; received November 21, 2021; accepted June 13, 2022

Cell migration in confined environments is fundamental for diverse biological processes from cancer invasion to leukocyte trafficking. The cell body is propelled by the contractile force of actomyosin networks transmitted from the cell membrane to the external substrates. However, physical determinants of actomyosin-based migration capacity in confined environments are not fully understood. Here, we develop an in vitro migratory cell model, where cytoplasmic actomyosin networks are encapsulated into droplets surrounded by a lipid monolayer membrane. We find that the droplet can move when the actomyosin networks are bound to the membrane, in which the physical interaction between the contracting actomyosin networks and the membrane generates a propulsive force. The droplet moves faster when it has a larger contact area with the substrates, while narrower confinement reduces the migration speed. By combining experimental observations and active gel theory, we propose a mechanism where the balance between sliding friction force, which is a reaction force of the contractile force, and viscous drag determines the migration speed, providing a physical basis of actomyosin-based motility in confined environments.

actin cytoskeleton | reconstituted systems | microfluidics | cell migration | active gels

Significance

Micrometer-scale small active systems, ranging from cells migrating through viscoelastic tissues to self-propelled droplets in microfluidic platforms, are often subject to environmental confinement. Growing evidence suggests that such confined environments are an essential factor to generate propulsive force, but its physical basis is still poorly understood. Here, by creating a simplified model of cell migration with active cytoskeleton enclosed in cell-sized droplets under confinement, we demonstrate that a propulsive force can be generated by the physical interaction between contracting active cytoskeleton and inner droplet surface. Furthermore, we show experimentally and theoretically that the force balance between propulsive force and confinement-induced viscous drag determines the migration speed, revealing a physical mechanism of the active cytoskeleton-based motility that utilizes environmental mechanical constraints.

One of the distinctive abilities of biological systems is the autonomous conversion of chemical energy into mechanical work, such as cell-shape deformation (1), cell migration (2, 3), and cytoplasmic streaming (4). A key player driving these mechanical processes is the actin cytoskeleton, which is mainly composed of actin filaments (F-actin) and myosin molecular motors, generating contractile forces coupled with adenosine triphosphate (ATP) hydrolysis (5). Notably, a unique feature of migratory cells is force transmission: Intracellular contractile forces are transmitted to the external environment via physical contact, by which the cell body is propelled forward (6). Growing evidence suggests that the actin cytoskeleton beneath the cell membrane is responsible for force transmission to the extracellular matrix via transmembrane adhesive proteins (7) or to the solid substrates, even without specific anchoring proteins (8).

Although much is known about molecular processes regulating cell migration, little is known about physical determinants responsible for efficient force transmission. This is because the inherent complexities of the cellular environment, such as complex actin–membrane interactions and membrane–substrate interactions via adhesive transmembrane proteins, obscure the mechanical contributions of contractile actomyosin networks to force transmission (6–8). Moreover, because of the regulation of actomyosin contractility through biochemical signaling, such as calcium-dependent mechanotransduction (9) and Hippo–YAP/TAZ pathways (10, 11), it is controversial whether the efficient force transmission is the fine-tuned output of the chemical signal processing or the optimal mechanical action of actomyosin networks. Hence, identifying the key physical determinants that achieve efficient force transmission remains a challenge.

To understand how actomyosin networks undergo a wide range of self-organization, simplified experimental model systems that separate the mechanics from biochemical signaling have been developed (12–14). In vitro reconstituted systems, such as purified actomyosin or actin-intact cytoplasmic extracts, are encapsulated into cell-sized compartments made of liposomes or water-in-oil droplets with defined actin–membrane interactions (15–17). These simplified experimental models offer versatile platforms to explore key physical determinants of self-organized actomyosin networks because one can specify the concentration of proteins, actin–membrane interactions, and membrane–substrate interactions. On the one hand, these compartmentalized actomyosin networks have revealed rich self-organization, ranging from spontaneous actin flow (18, 19) to positioning control of subcellular large bodies (20, 21). On the other hand, the mechanics of actomyosin networks interacting with the membrane and dynamically exerting forces in a cell-sized compartment are far from being understood. To gain insights into a unified framework of actomyosin-based motility from in vitro models to living cells, one needs to explore how interfacial actomyosin networks enable force transmission,

Author contributions: R.S. and Y.T.M. designed research; R.S. and Y.T.M. performed research; R.S., Z.I., Y.S., M.M., and Y.T.M. contributed new reagents/analytic tools; R.S. analyzed data; and R.S. and Y.T.M. wrote the paper.

The authors declare no competing interest.

This article is a PNAS Direct Submission.

[1]To whom correspondence may be addressed. Email: sakaryo@phys.kyushu-u.ac.jp or ymaeda@phys.kyushu-u.ac.jp.

This article contains supporting information online at https://www.pnas.org/lookup/suppl/doi:10.1073/pnas.2121147119/-/DCSupplemental.

Published July 20, 2022.

as well as the influence of external physical constraints on self-propulsion, such as fluid drag and confinement geometry.

Here, we report an in vitro migratory cell model undergoing self-propulsive migration, in which cytoplasmic actomyosin networks are encapsulated in cell-sized water-in-oil droplets covered with a lipid monolayer membrane. By implementing the binding of F-actin to the membrane interface, we reconstructed cell-like polarization and actin flow. This actin flow efficiently transmits its contractile force across the membrane via actin–membrane binding and through substrate contact, which drives the droplet migration. Moreover, the migration of actomyosin droplets under two-dimensional (2D) confinement is highly directed and gets faster with efficient force transmission. We explained the migration mechanism based on active gel theory by considering a force balance between sliding friction force, which is a reaction force of the contractile force, and viscous drag, allowing us to set the founding ground to control migration capacity through environmental geometry. Our approach is, thus, a simple, yet generic, strategy for studying active force transmission without the help of signaling pathways or transmembrane adhesions, granting a mechanistic understanding of actomyosin-based motility in confined environments.

Results

Confined Polarized Actomyosin Networks Drives Actomyosin Droplet Migration. Here, we built an in vitro model of actomyosin-driven migration by encapsulating *Xenopus laevis* egg extracts containing physiological concentrations of actin and myosin into water-in-oil droplets (hereafter called "actomyosin droplets"). First, poly-dispersed actomyosin droplets were confined between polydimethylsiloxane (PDMS)-coated glass slides (Fig. 1*A*). The droplets were covered with a lipid monolayer membrane, ensuring that there was neither specific substrate adhesion nor anchoring between the droplets and the substrates. F-actin was nucleated by the Arp2/3 complex (12, 20) and distributed uniformly inside the droplets, visualized by tetramethylrhodamine (TMR)-labeled Lifeact bound to F-actin filaments (22) (Fig. 1 *B* and *C*, control). To bind F-actin to the membrane, we added a phospholipid L-α-phosphatidyl-D-myo-inositol-4,5-bisphosphate (PIP_2), which is known to recruit actin–cross-linking proteins (23, 24) and promote F-actin assembly by activating Arp2/3 (25–29). Indeed, F-actin was localized beneath the membrane interface by adding PIP_2 (Fig. 1 *B* and *C*, +PIP_2). We confirmed by fluorescence recovery after photo bleaching (FRAP) that G-actin replacement is delayed near the membrane boundary in the presence of PIP_2, which also reflects the localization of Arp2/3-dependent F-actin network (Fig. 1*D* and *SI Appendix*, Fig. S1).

The polymerized actomyosin network and membrane-bound F-actin did not remain stable, but started to contract $\sim$20 s after substrate confinement (Fig. 1 *E* and *F*). The actomyosin network without actin–membrane binding was contracted toward the center (Fig. 1 *E* and Movie S1), consistent with our previous study (20). In contrast, the actomyosin network with actin–membrane binding dissociated from the membrane interface and contracted toward the facing periphery (Fig. 1*F* and Movie S1). The spatial distribution of the actomyosin network was quantified by the asymmetry parameter Φ_{asym}, which is defined as the distance between the droplet centroid and the center of mass of F-actin distribution normalized by the major axis length of the droplet (Fig. 1*G*). Without actin–membrane binding, the asymmetry parameter remained small ($\Phi_{\mathrm{asym}} = 0.15$), whereas with actin–membrane binding, the asymmetry parameter increased to $\Phi_{\mathrm{asym}} = 0.50$ within 2 min and then reached a plateau (Fig. 1*H*).

Surprisingly, with actin–membrane binding, actomyosin droplets started to migrate immediately after the polarization of actomyosin distribution, accompanied by dynamic shape deformation (Fig. 1 *I* and *J* and Movies S2 and S3). The actin flow contracted from the front to the rear of the migrating droplet (Fig. 1*K*). Shape deformation was prominent at the rear, where contractile actomyosin accumulated. The actin flow reflects a contractile force gradient along the droplet polarity, which is the key to propelling the droplet. We confirmed that the physical interaction of either F-actin cross-linker α-actinin or an activator of the Arp2/3-mediated F-actin polymerization, VVCA (Verprolin, cofilin, acidic) domain of N-WASP, with the droplet interface also enabled droplet migration (*SI Appendix*, Figs. S2 and S3 and Movie S4). This suggests that the physical interaction of F-actin with the membrane interface is crucial for actomyosin droplet migration.

To test the contribution of actin polymerization and the contraction to the establishment of the actin flow and the droplet migration, we performed the molecular perturbations for the inhibition of the Arp2/3 complex and myosin. Inhibition of the Arp2/3 complex by CK666 significantly decreased both the migration speed and the actin-flow speed, indicating that the lower density of polymerized actin decreased the net contractility of the actomyosin network (Fig. 1 *L* and *M*, *SI Appendix*, Fig. S4, and Movie S5). In addition, the inhibition of the myosin contractility by Y27632 significantly decreased both the migration speed and the actin-flow speed (Fig. 1 *L* and *M*, *SI Appendix*, Fig. S4, and Movie S5). The slower droplet speed under these molecular perturbations suggests the contribution of the actin flow to the propulsion force generation. Together, these molecular perturbations demonstrate the importance of the contraction and the polymerization on the establishment of the actin flow and the movement of the droplets.

We estimated the efficiency of gaining motility by analyzing the number fraction of the migrating and immotile droplets (*SI Appendix*, Fig. S5 and Movie S6). We found 66% of migrating droplets, whereas there were 34% of immotile droplets, even in the presence of actin–membrane binding, and they were classified into two cases: 1) 28% of the droplets could not form the polarity of the actomyosin distribution, or 2) 6% of the droplets in which the actomyosin network could not initially contract because the contractility of the actomyosin network could not outweigh the strength of actin–membrane binding (*SI Appendix*, Fig. S5). In the case of droplets (1), the high-density actomyosin cluster was contracted toward the center of the droplet, and, thus, it lost the polarity. In the case of droplets (2), the actomyosin network formed a uniform cortex, which had neither polarity nor actin flow. Thus, these results suggest that the establishment of polarity and the generation of contractile force are important conditions to induce droplet migration.

Polarization of Actomyosin Networks Alone Is Not Sufficient to Propel the Droplet. With actin–membrane binding, actomyosin droplets exhibited polarization and migration, while neither polarization nor migration was observed without actin–membrane binding (Fig. 2*A*). To clarify the role of polarity in migration capacity, we magnetically manipulated the actomyosin networks: Magnetic beads injected into the extracts were accumulated at the center of the droplet by the contracted actomyosin gel; thus, the position of the gel-like structure and polarization can be manipulated by an external magnetic field (21) (Fig. 2 *B* and *C* and Movie S7). Here, the polarization of actomyosin networks was initially built by using a magnetic force that was thereafter turned off, and images were acquired. The initially induced

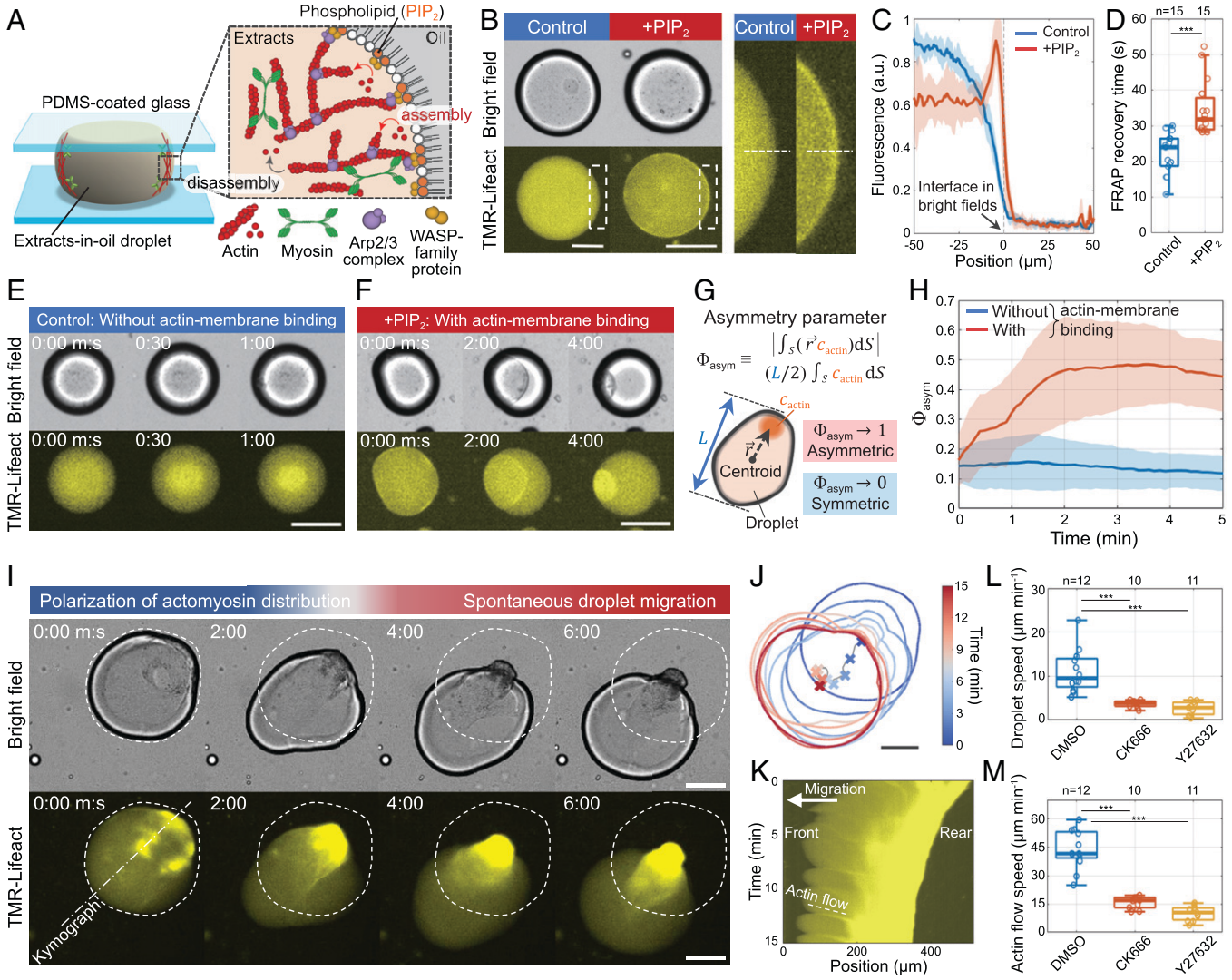

Fig. 1. Polarized F-actin distribution induces the spontaneous migration of confined extracts-in-oil droplets. (*A*) Schematic of the experimental setup. Extracts-in-oil droplets were confined between PDMS-coated glass slides. F-actin is polymerized by the Arp2/3 complex, which is activated by the WASP-family protein beneath the lipid membrane in the presence of PIP_2, while the myosin motors induce contractile stress. F-actin is bound to the lipid monolayer interface, depending on the composition of the phospholipids (i.e., PIP_2). (*B*) Snapshots of extracts-in-oil droplets showing PIP_2-dependent localization of F-actin at the droplet surface. (*B*, *Right*) The membrane interface within white dashed boxes is magnified. F-actin is labeled with TMR-Lifeact. (*C*) Spatial profiles of F-actin fluorescence across the membrane interface along the dashed lines in *B* in control (n = 8; in blue) and with PIP_2 ($n = 14$; in red). A.u., arbitrary units. (*D*) Box plot showing the FRAP recovery time of Alexa Fluor 546-labeled actin in the vicinity of the membrane interface in control ($n = 15$; in blue) and +PIP_2 ($n = 15$; in red). ***$P < 0.001$) (Mann–Whitney u test,) (*SI Appendix*, Fig. S1). (*E* and *F*) Time sequence of actomyosin contraction (Movie S1). (*E*) Actomyosin contraction without actin–membrane binding (control). (*F*) Actomyosin contraction with actin–membrane binding (+PIP_2). (*G*) Asymmetry parameter Φ_{asym} is defined as the center of mass of the F-actin distribution inside the droplet S, normalized by the length of the droplet long-axis L. The larger asymmetry parameter indicates that F-actin is accumulated near the boundary. (*H*) Time evolution of Φ_{asym} without actin–membrane binding (n = 10; in blue) and with actin–membrane binding ($n = 17$; in red). Data are mean ± SD. (*I*) Time sequence of the polarization of actomyosin distribution and the following droplet migration under the height of 60-μm chamber (Movies S2 and S3). The white dashed lines represent the initial droplet boundary. (*J*) Droplet boundary analyzed from *I*. Time is color-coded. (*K*) Kymograph of a migrating droplet measured at the dotted broken line in *I*. (*L*) Box plot showing the droplet speed averaged for 5 min with dimethylsulfoxide (DMSO) ($n = 12$; in blue), 2 mM CK666 ($n = 10$; in red), and 2 μM Y27632 ($n = 11$; in yellow). ***$P < 0.001$ (Mann–Whitney u test,). (*M*) Box plot showing the actin-flow speed with DMSO ($n = 12$; in blue), 2 mM CK666 ($n = 10$; in red), and 2 μM Y27632 ($n = 11$; in yellow). ***$P < 0.001$ (Mann–Whitney u test). The efficiency of gaining motility was estimated based on the fraction of migrating droplets: 63% of migrating droplets out of 19 droplets (DMSO), 56% of migrating droplets out of 18 droplets (CK666), and 52% of migrating droplets out of 21 droplets (Y27632). Droplets of diameter within $110 < D < 200$ μm were analyzed under the height of $h = 100$ μm chamber. All images were taken by epifluorescence microscopy. (Scale bars, 100 μm.)

polarization was comparable between actomyosin droplets with actin–membrane binding ($\Phi_{asym} = 0.54 \pm 0.19$ at 0 min, mean ± SD) and without actin–membrane binding ($\Phi_{asym} = 0.50 \pm 0.08$ at 0 min) (Fig. 2*D*). However, only the droplets with actin–membrane binding showed migration (Fig. 2*E* and Movie S8). Furthermore, nonpolarized actomyosin droplets with actin–membrane binding recovered their migration capacity by magnetic force-induced polarization (Fig. 2*F* and Movie S9; a magnetic force was kept applied). These results indicate that polarity alone is not sufficient to drive droplet migration, but actin–membrane binding is essential for generating a propulsion force.

Actomyosin Contractility Is Transmitted to the Substrate via Actin–Membrane Binding. To provide evidence of the force transmission of actin flow via actin–membrane binding, we performed force-transmission microscopy inspired by Abercrombie's seminal study on cell migration (30). After spreading tracer silica beads onto the bottom substrate, actomyosin droplets were placed on the beads carpet (Fig. 3*A*). We reasoned that if the actin flow transmits the contractile force to the external environment, it could move the objects in contact with the outside of the membrane. Indeed, the beads moved with the actin flow only under the droplets with actin–membrane binding (Fig. 3 *B* and *C*,

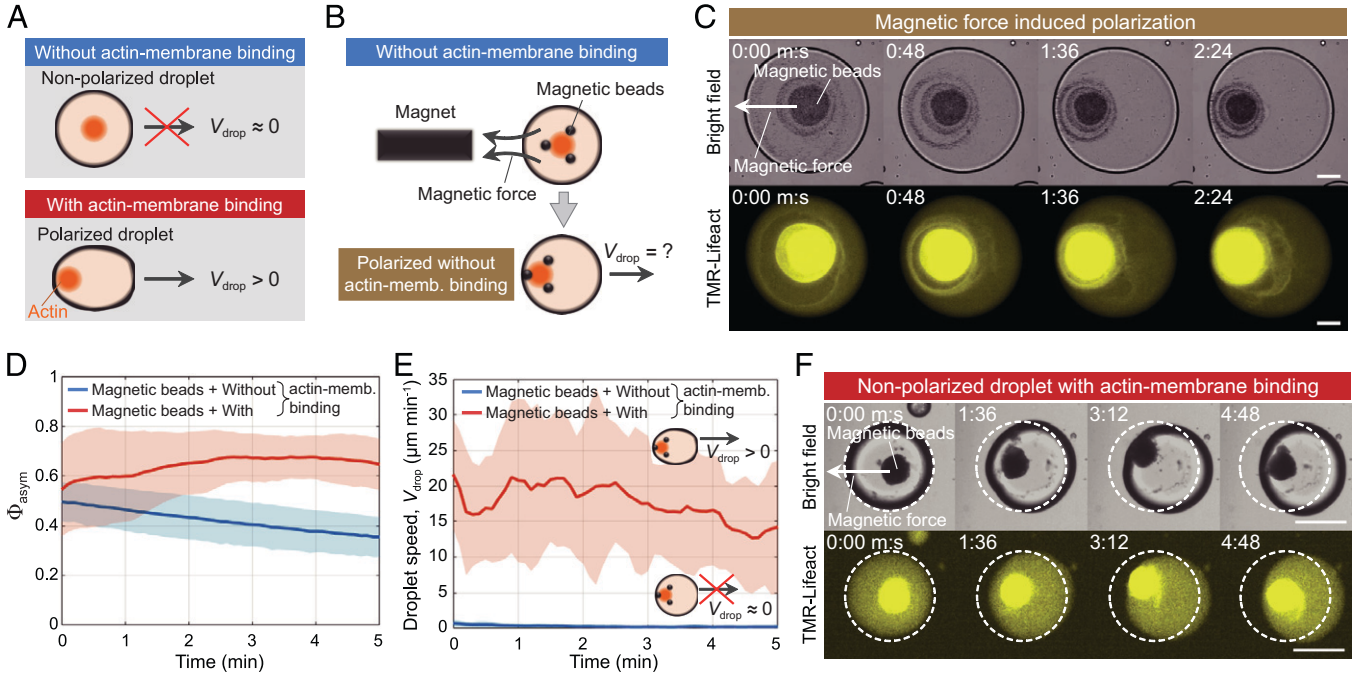

Fig. 2. Polarization of actomyosin networks alone is not sufficient to drive actomyosin droplet migration. (*A*) Schematic summarizing the effect of actin–membrane binding on polarity and migration speed V_{drop}. (*B*) Schematic of the magnetic force-induced polarization. Polarization is induced by applying the magnetic force on magnetic beads entangled with the actomyosin networks. (*C*) Time sequence of magnetic force-induced polarization (Movie S7). (*D*) The asymmetry parameter Φ_{asym} without actin–membrane (memb.) binding ($n = 10$; in blue) and with actin–membrane binding ($n = 15$; in red). Data are mean ± SD. (*E*) Droplet speed after polarity induction without actin–membrane binding ($n = 10$; in blue) and with actin–membrane binding ($n = 15$; in red) (Movie S8). Data are mean ± SD. The efficiency of gaining motility was estimated to be 60% based on the fraction of migrating droplets out of 25 droplets. (*F*) Time-lapse images showing a droplet with actin–membrane binding that initially had no polarity started to migrate after magnetic force-induced polarization (Movie S9). The white dashed lines represent the initial droplet boundary. All images were taken by epifluorescence microscopy. (Scale bars, 100 μm.)

SI Appendix, Fig. S6, and Movie S10). These results demonstrate that the contractile force of actin flow is transmitted to the external environment via actin–membrane binding.

We then hypothesized that the total contractile force transmitted to the external substrates would depend on the contact area between the droplet and the substrates. To test this, we analyzed the droplet size dependence of the movement of the beads. We found that the total number of moving beads was increased for the larger droplets, suggesting that the total contractile force transmitted to the external substrates is increased with the contact area such that $F_{act}^{contact} \propto \pi R_c^2$, where R_c is the contact radius (*SI Appendix*, Fig. S7). On the other hand, the speed of the moving beads was not correlated with the droplet size, suggesting that the locally transmitted contractile force per unit area σ_{act} is independent of the contact area (*SI Appendix*, Fig. S7). Notably, the beads' speed was positively correlated with the actin-flow speed (*SI Appendix*, Fig. S7), indicating that the locally transmitted contractile force per unit area is predominantly determined by the actin-flow speed, such that $\sigma_{act} = \alpha v_{act}$, where α is the geometry-independent friction coefficient, and v_{act} is the actin-flow speed. Since the passive sliding friction force acts on the droplet as a reaction force of this contractile force, the total sliding friction force $F_{fric}^{contact}$ is proportional to the contact area, $F_{fric}^{contact} \propto \pi R_c^2$, by which the droplet is self-propelled (Fig. 3*D*). Based on these results, we propose the sliding friction force $F_{fric}^{contact}$ as a propulsion force of the migrating droplet.

Substrate Confinement Enables Highly Directed Actomyosin Droplet Migration. The interfacial sliding friction force implies that the contact area between the droplet and the substrate could modulate the migration capacity. To test this, we compared the migration speed of the confined droplets with that of unconfined droplets (Fig. 3*E*). Without actin–membrane binding, migration was not observed for both unconfined and confined actomyosin droplets (Fig. 3 *F*, *Left*). Notably, with actin–membrane binding, the migration speed of confined droplets was ∼4 times faster than that of unconfined droplets (Fig. 3 *F*, *Right*), indicating that the substrate contact under confinement efficiently transmits the contractile force. Confocal microscopy confirmed that the contact area remained constant during migration (*SI Appendix*, Fig. S8 and Movies S11 and S12). In addition, the mean-square displacement (MSD) of the unconfined droplets showed diffusive motion, whereas the confined droplets showed ballistic motion (Fig. 3*G* and Movie S13). The droplet polarity, defined as the direction from the center of mass of F-actin toward the droplet centroid, showed that its angle fluctuation was small in both confined and unconfined droplets, and the time correlation of polarity was maintained for ∼10 min (Fig. 3*H*; orange, correlation time $\tau_c = 547$ s for unconfined and $\tau_c = 818$ s for confined; *SI Appendix*, Fig. S9). In contrast, the trajectories of unconfined droplets were randomly distributed, whereas those of confined droplets were mostly oriented in the same direction as the polarity (Fig. 3*H*, gray; correlation time $\tau_c = 51$ s for unconfined and $\tau_c = 432$ s for confined; *SI Appendix*, Fig. S9). These results suggest that the polarity of actomyosin distribution is inherently stable, but to navigate the droplet to the direction of stable polarity, sliding friction force imposed by the confinement is necessary. Taken together, substrate contact controls droplet migration by not only transmitting the contractile force of actin flow to the substrate, but also by stably orientating the contractile force along the polarity.

Confinement Geometry Controls the Migration Speed of Actomyosin Droplets. We identified two key elements of force transmission: 1) actin–membrane binding and 2) substrate contact. Based on these results, we propose a model of actomyosin droplet

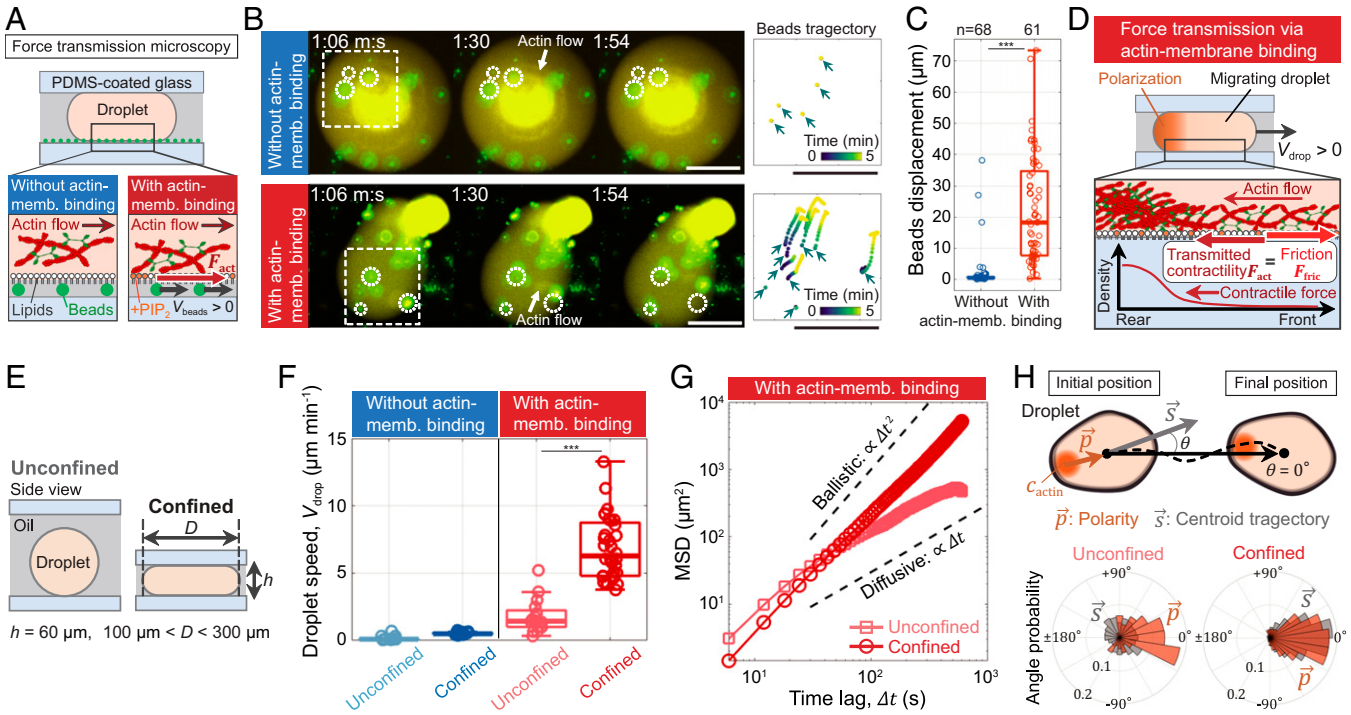

Fig. 3. Force transmission via actin–membrane binding and through substrate contact enables actomyosin droplet migration. (*A*) Schematic of the force-transmission microscopy. Beads are displaced by the actin flow when the contractile force of actin flow F_{act} is transmitted to the bottom substrate. (*B*) Time sequence of beads transport by actin flow without actin–membrane binding (*Upper*) and with actin–membrane binding (*Lower*) (Movie S10). The white dotted circles represent the initial position of the beads. (*B, Right*) Beads in the white dashed boxes were tracked. Initial bead positions are indicated by blue arrows. The chamber height was 100 μm. (*C*) Bead displacement for 5 min without actin–membrane binding ($n = 68$ beads under 6 droplets; in blue) and with actin–membrane binding ($n = 61$ beads under 10 droplets; in red). ***$P < 0.001$ (Mann–Whitney u test). The efficiency of gaining motility was estimated to be 62% based on the fraction of migrating droplets out of 26 droplets (*SI Appendix*, Fig. S7). (*D*) Schematic showing droplet-migration mechanism. Polarized actomyosin sustains the rearward actin flow. The contractile force of actin flow F_{act} is transmitted to the substrate via actin–membrane binding, by which counteracting sliding friction force F_{fric} is generated. (*E*) Schematic showing unconfined and confined droplets. Droplets of diameter within $100 < D < 300$ μm were analyzed at the chamber height of $h = 60$ μm for confined and $h = 300$ μm for unconfined. (*F*) Average droplet speed for 10 min without actin–membrane binding for unconfined ($n = 22$; in light blue) and confined ($n = 17$; in blue) droplets and with actin–membrane binding for unconfined ($n = 16$; in light red) and confined ($n = 32$; in red) droplets ***$P < 0.001$ (Mann–Whitney u test). (*G*) MSD of droplet centroids with actin–membrane binding for unconfined ($n = 16$; in light red) and confined ($n = 32$; in red) droplets (Movie S13). (*H*) Angle probability of the trajectory ($\vec{s}$; in gray) and polarity ($\vec{p}$; in orange) for unconfined ($n = 16$; *Left*) and confined ($n = 32$; *Right*) droplets. The angle of the trajectory and polarity is measured from the straight line between the initial and final droplet position. The polarity of the droplet is defined as the direction from the center of mass of F-actin to the droplet centroid. The efficiency of gaining motility was estimated based on the fraction of migrating droplets: 67% of migrating droplets out of 24 unconfined droplets and 69% of migrating droplets out of 45 confined droplets. All images were taken by epifluorescence microscopy. (Scale bars, 100 μm.) Memb., membrane.

migration under 2D confinement by considering the force balance over the droplet surface. On the one hand, F-actin bound to the membrane forms actomyosin gel, which contracts from the front to the rear of the migrating droplet, thereby inducing shear stress to the membrane interface at the contact area. Because of the force balance across this interface, the sliding friction force exerted by the substrate $F_{\mathrm{fric}}^{\mathrm{contact}}$ acts in the opposite direction to the actin flow (Fig. 3*D*). On the other hand, the shear stress at the lateral membrane interface $F_{\mathrm{fric}}^{\mathrm{lateral}}$ can be neglected because the viscosity of the surrounding oil is much smaller than that of the actomyosin gel [$\eta_{\mathrm{oil}}/\eta_{\mathrm{act}} \ll 1$ (31, 32)]. Therefore, the sliding friction force $F_{\mathrm{fric}}^{\mathrm{contact}}$ propels the droplet forward by balancing with the drag force F_{drag} from the surrounding oil when there is sufficient contact between the droplet and the substrate. Thus, the force balance is given by

$$F_{\mathrm{fric}}^{\mathrm{contact}} + F_{\mathrm{drag}} = 0, \qquad [1]$$

which determines the migration speed of the droplet.

Given that a droplet with a conserved volume is confined between substrates, stronger confinement would induce a faster migration because the total sliding friction force is proportional to the contact area, $F_{\mathrm{fric}}^{\mathrm{contact}} \propto \pi R_c^2$, where R_c is the contact radius. However, Stokes' hydrodynamics dictates that fluid drag increases with the stronger confinement because of a larger viscous dissipation, $F_{\mathrm{drag}} \propto \eta_{\mathrm{oil}} \nabla^2 v_{\mathrm{oil}}$, where η_{oil} and v_{oil} are the viscosity and velocity of the surrounding oil, respectively. Thus, examining this competition between propulsive and resistive forces is key to understanding migration under spatial constraints.

To test this geometric effect, we altered the chamber height at $h = 30,60,100$ μm and the droplet diameter from $D = 80$ μm to $D = 650$ μm (Fig. 4*A*). On the one hand, the migration speed varied from 0.5 $\mu\mathrm{m} \cdot \mathrm{min}^{-1}$ to 23 $\mu\mathrm{m} \cdot \mathrm{min}^{-1}$, where the migration speed increased with the droplet size at any chamber height (Fig. 4*A* and *SI Appendix*, Fig. S10). This indicates that a larger contact area induces a larger propulsive force, consistent with the theoretical prediction and force-transmission microscopy (*SI Appendix*, Fig. S7). On the other hand, the droplet speed averaged within $100 \leq D \leq 200$ μm had a peak at $h =$ 60 μm (Fig. 4*B* and *SI Appendix*, Fig. S10). This nonmonotonic height dependence indicates that a stronger confinement does not necessarily induce faster migration; instead, there is an optimal geometry. We confirmed that droplet speed did not significantly correlate with actin-flow speed (*SI Appendix*, Fig. S11), suggesting that the geometry dependence of droplet speed predominantly

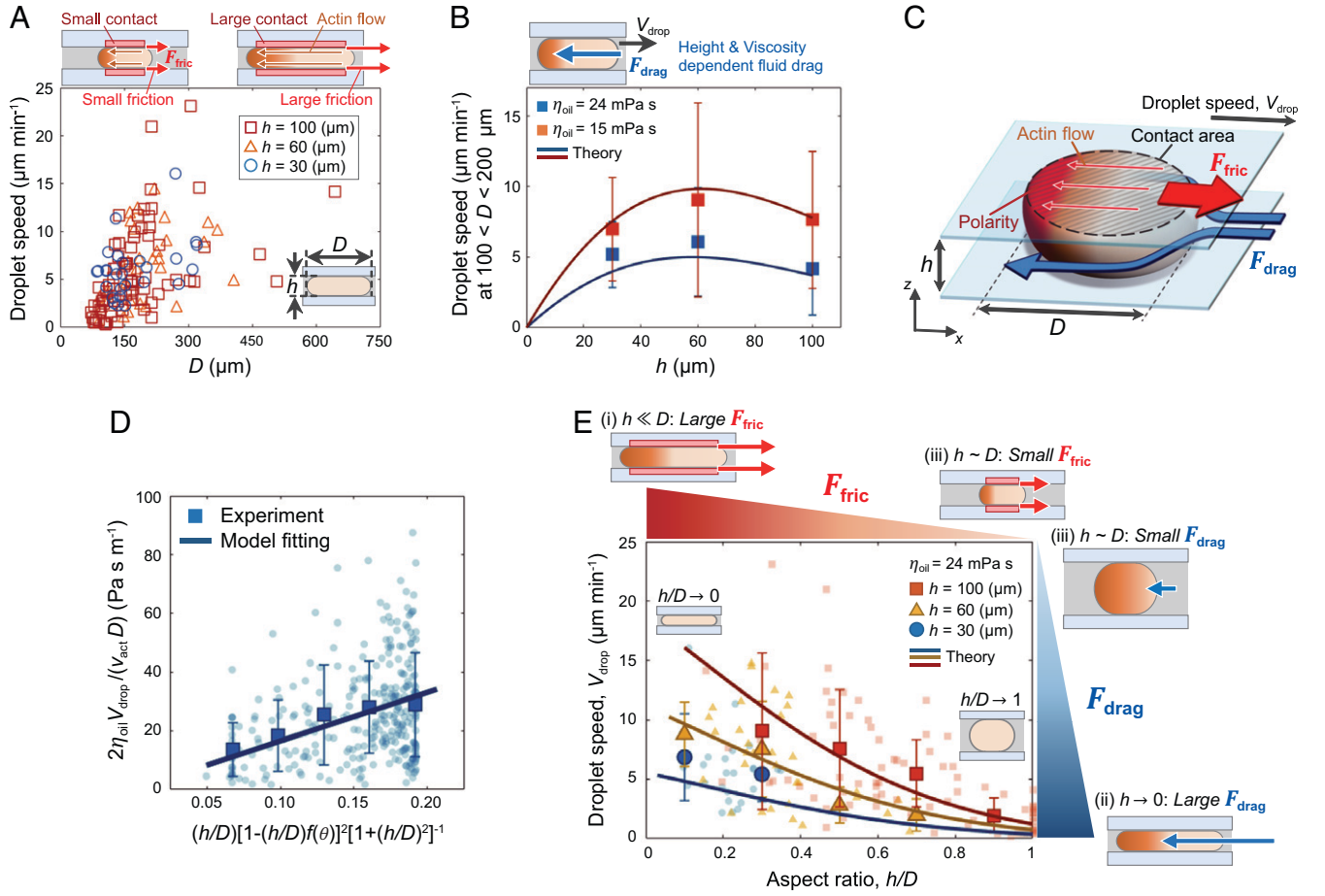

Fig. 4. Geometric dependence of migration speed and physical model of actomyosin droplet migration under 2D confinement. (*A*) Droplet size dependence of the migration speed under $h = 30$ μm ($n = 27$; blue circles), $h = 60$ μm ($n = 32$; yellow triangles), and $h = 100$ μm ($n = 77$; red squares). (*A*, *Inset*) Schematic shows the definition of height h and diameter D of the confined droplet. (*B*) Height dependence of the droplet speed averaged within $100 \leq D \leq 200$ μm under high-viscosity oil ($\eta_{oil} = 24$ mPa · s; in blue; $n = 18$ at $h = 30$ μm, $n = 15$ at $h = 60$ μm, and $n = 56$ at $h = 100$ μm) and low-viscosity oil ($\eta_{oil} = 15$ mPa · s; in orange; $n = 10$ at $h = 30$ μm, $n = 36$ at $h = 60$ μm, and $n = 55$ at $h = 100$ μm). Data are mean ± SD. Solid lines correspond to the theoretical model with averaged droplet diameter $D \simeq 140$ μm for $\eta_{oil} = 24$ mPa · s and $D \simeq 148$ μm for $\eta_{oil} = 15$ mPa · s (*SI Appendix*, Fig. S10). (*C*) Schematic summarizing the mechanism of actomyosin droplet migration. Given that a droplet of diameter D with migration speed V_{drop} is confined under 2D confinement of height h, which is propelled by the sliding friction force F_{fric} induced by actin flow and the droplet experiences drag force F_{drag} from the surrounding oil. (*D*) Geometric scaling of Eq. **2**. The scatterplot shows individual data ($n = 305$), and squares show binned averaged data with mean ± SD. The solid lines show the linear fitting to the experimental data, which yielded $\alpha = 1.7 \times 10^2$ Pa · s · m^{-1}. (*E*) Aspect ratio h/D dependence of the migration speed under high-viscosity oil ($\eta_{oil} = 24$ mPa · s). The scatterplot shows individual data for $h = 30$ μm ($n = 27$; blue circles), $h = 60$ μm ($n = 32$; yellow triangles), and $h = 100$ μm ($n = 77$; red squares), and larger symbols show binned averaged data with mean ± SD. Solid lines correspond to the theoretical model. Schematic shows geometry-dependent migration speed. At a fixed chamber height, migration speed increases with the droplet size because of the associated increase of the sliding friction force outweighs that of the fluid drag [(*i*) $h \ll D$]. Because the competing forces scale as $F_{drag} \propto h^{-2}$ and $F_{fric} \propto \pi R_c^2 \propto h^{-1}$, as the chamber height decreases [(*ii*) $h \to 0$], the increase of the fluid drag outweighs that of the sliding friction force. Conversely, as chamber height becomes close to the droplet diameter [(*iii*) $h \sim D$], both the sliding friction force and fluid drag decreases. The efficiency of gaining motility was estimated to be 65% based on the fraction of migrating droplets out of 213 droplets (*SI Appendix*, Fig. S5).

originates from contact with the substrate. The contribution of fluid drag was also confirmed by decreasing the viscosity of the surrounding oil from $\eta_{oil} = 24$ mPa · s to $\eta_{oil} = 15$ mPa · s, resulting in a faster migration speed (Fig. 4*B* and *SI Appendix*, Fig. S10).

Geometric Balance Between Sliding Friction Force and Fluid Drag Determines Migration Speed. To understand the geometry-dependent migration speed, we considered a theoretical model of a migrating actomyosin droplet confined between 2D substrates, where actomyosin networks are described as active gels (3, 5, 32) (*SI Appendix*, section 1). For simplicity, we assumed a circular droplet shape because the ratio of the major and minor axis lengths of the droplets was ≃0.87 (*SI Appendix*, Fig. S12 and section 2). Here, we considered a droplet migrating along its polarity axis at a speed of V_{drop} (Fig. 4*C*). With actin–membrane binding, actin flow generates shear stress at the membrane interface, $\sigma_{act} = \alpha v_{act}$, where v_{act} is the actin-flow speed and α is the friction coefficient. The force balance across the membrane interface dictates that the sliding friction force from the substrate $F_{fric}^{contact}$ acts in the opposite direction to the actin flow, by which the actomyosin droplet is propelled forward (Figs. 3*D* and 4*C*).

Next, we derived the geometry dependence of V_{drop} from the force-balance condition in Eq. **1**. On the one hand, the total sliding friction force is obtained by integrating the actin-flow-induced shear stress over the contact area, $F_{fric}^{contact} = -2\int \sigma_{act} dS \simeq -2(\alpha v_{act})(\pi R_c^2)$, where $R_c \equiv R - (h/2)f(\theta)$ is the contact radius, R is the droplet radius, $f(\theta) = -(|\tan\theta| + 1/\cos\theta)$ is the geometric constant, and $\theta = 154.7°$ is the contact angle at the droplet–substrate interface (*SI Appendix*, Fig. S13). On the other hand, the drag force is given by $F_{drag} \simeq \eta_{oil}\nabla^2 v_{oil}(\pi R^2 h) \sim \eta_{oil}\left[(D/2)^{-2} + (h/2)^{-2}\right] V_{drop}[\pi (D/2)^2 h]$ because the velocity gradient in the surrounding fluid across both droplet radius and chamber height contributes to viscous dissipation (33). Thus, the migration speed is given by

$$V_{\mathrm{drop}} = \frac{\alpha v_{\mathrm{act}}}{2\eta_{\mathrm{oil}}} h \left(1 + \left(\frac{h}{D}\right)^2\right)^{-1} \left(1 - \frac{h}{D} f(\theta)\right)^2. \quad [2]$$

To obtain the geometry-independent friction coefficient α, we scaled the droplet speed to $2\eta_{\mathrm{oil}} V_{\mathrm{drop}}/(v_{\mathrm{act}} D)$ using $\eta_{\mathrm{oil}} = 24$ mPa·s with $v_{\mathrm{act}} \simeq 54$ μm·min^{-1} and $\eta_{\mathrm{oil}} = 15$ mPa·s with $v_{\mathrm{act}} \simeq 62$ μm·min^{-1} (*SI Appendix*, Fig. S11). This geometric scaling was observed in the experimental data, where a linear fitting yielded $\alpha = 1.7 \times 10^2$ Pa·s·m^{-1} (Fig. 4*D*). We estimated the friction stress $F_{\mathrm{fric}}^{\mathrm{contact}}/(2\pi R_{\mathrm{c}}^2) \simeq \alpha v_{\mathrm{act}} \simeq 0.16$ mPa (*SI Appendix*, section 1), which is several times smaller than the friction stress $\lesssim 1$ mPa of migrating cells in confined spaces (32). Notably, using only one obtained parameter α, this model reproduced the geometric dependence of the droplet speed well (Fig. 4 *B* and *E* and *SI Appendix*, Fig. S10).

We can now explain how the confinement geometry influences the migration speed (Fig. 4*E*). Here, as the aspect ratio h/D approaches one, the droplet shape becomes closer to that of a sphere, while the droplet shape resembles that of a pancake at a smaller aspect ratio. On the one hand, at a fixed chamber height, the migration speed is increased for larger droplets because of the larger sliding friction force [(*i*) $h \ll D$]. On the other hand, the migration speed decreases for a smaller chamber height [(*ii*) $h \to 0$]. This is because, given that a droplet with a conserved volume $\pi R^2 h = \mathrm{const.}$ is confined in a thin space, the height dependences of the sliding friction force and fluid drag are represented as $F_{\mathrm{drag}} \propto h^{-2}$ and $F_{\mathrm{fric}}^{\mathrm{contact}} \propto \pi R_{\mathrm{c}}^2 \propto h^{-1}$, respectively. Therefore, at a smaller chamber height, the increase in the sliding friction force is unable to compensate for the larger fluid drag, resulting in a slower migration speed. Conversely, when the chamber height is close to the droplet diameter [(*iii*) $h \sim D$], although the fluid drag becomes smaller, the sliding friction force also decreases; thus, the migration speed inevitably decreases. Together, this trade-off between sliding friction force, which is a reaction force of the contractile force, and fluid drag determines the migration capacity of actomyosin droplets in confined environments.

Actomyosin Droplet Can Migrate through Quasi-One-Dimensional Annulus Microchannels. To untangle the contribution of sliding friction force underlying this trade-off relation, we employed confinement within one-dimensional (1D) microchannels that allows us to increase the propulsive force without changing the fluid drag (i.e., cross-sectional area) (Fig. 5*A*). The droplets confined in the quasi-1D annulus PDMS microchannels were in complete contact with the wall, so that spontaneous shape deformation was suppressed, except at the trailing end (Fig. 5*B*). Droplet migration in microchannels suggests that it is predominantly driven by actin flow (Fig. 5 *B* and *C* and Movie S14). By using channel widths of $w = 100$ μm and $w = 150$ μm with a fixed height of $h = 60$ μm and the major axis length of the droplets L from 125 μm to 520 μm, the migration speed varied from 2.6 μm·min^{-1} to 12.9 μm·min^{-1} (Fig. 5 *D* and *E*), whereas the droplet speed did not significantly correlate with the actin-flow speed (*SI Appendix*, Fig. S14). The theoretical fitting of the geometric scaling yielded the friction stress $\alpha v_{\mathrm{act}} \simeq 0.26$ mPa (Fig. 5*F* and *SI Appendix*, section 3). Thus, friction-driven migration provides the same extent of propulsion force as in 2D confinement, regardless of the complexity of spatial confinement. The migration speed was ∼1.8 times larger at a smaller aspect

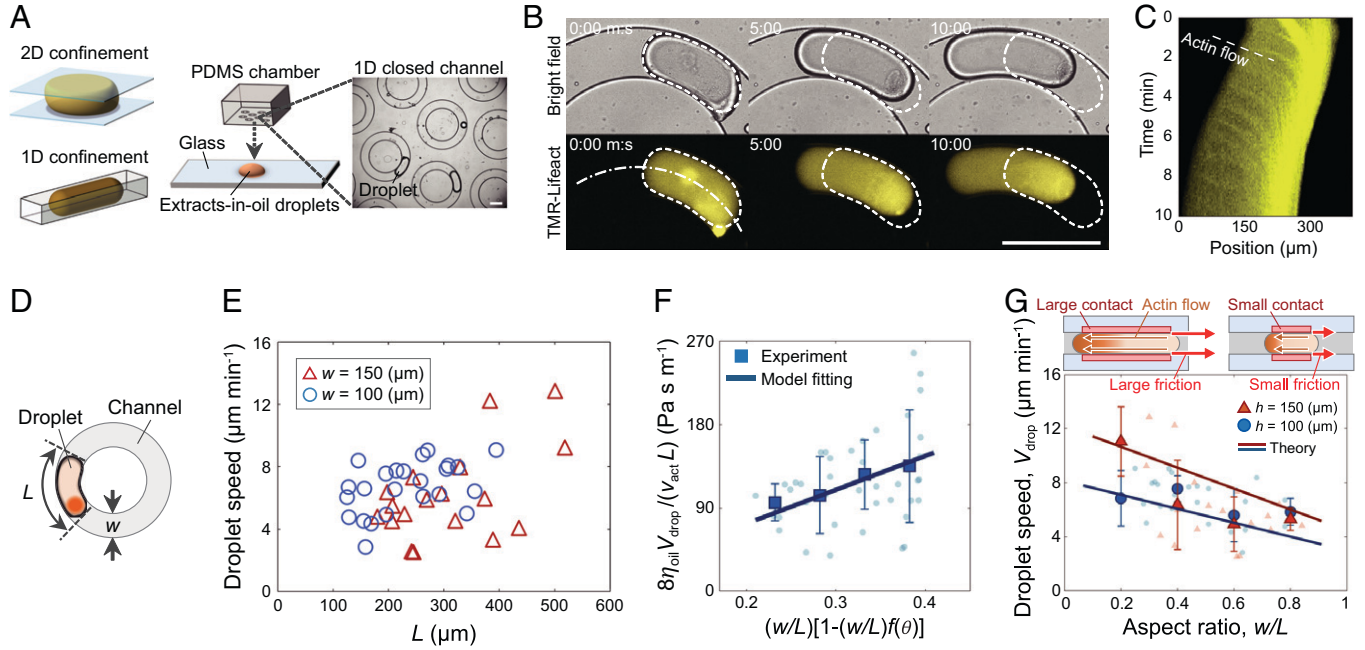

Fig. 5. Actomyosin droplet migration under 1D confinement. (*A*) Schematic showing 2D and 1D confinement with the experimental setup. The 1D closed-channel patterns are designed at the PDMS chamber, which is placed onto extracts-in-oil droplets. The zoom-in view shows a representative image of droplets confined in 1D closed channels. (*B*) Time sequence of a droplet migration under 1D confinement with the channel width of 100 μm and height of 60 μm (Movie S14). The white dashed lines represent the initial boundary of the droplet. (*C*) Kymograph of the actin flow extracted from the white dotted broken line in *B*. (*D*) Schematic showing the channel geometry defined by the width w, and the major axis length of the droplet is L. Channel height is fixed as 60 μm. (*E*) Droplet length dependence of the droplet speed under $w = 100$ μm ($n = 24$; blue circles) and $w = 150$ μm ($n = 18$; red triangles). (*F*) Geometric scaling of *SI Appendix*, Eq. **5** (*SI Appendix*, section 3). The scatterplot shows individual data ($n = 42$), and squares show binned averaged data with mean ± SD. The solid lines show the linear fitting to the experimental data, which yielded $\alpha = 3.6 \times 10^2$ Pa·s·m^{-1}. (*G*) The aspect ratio w/L dependence of droplet speed in 1D closed channel. The scatterplot shows individual data for $w = 100$ μm ($n = 24$; blue circles) and $w = 150$ μm ($n = 18$; red triangles), and larger symbols show binned averaged data with mean ± SD. Solid lines correspond to the theoretical model. The schematic in *G*, *Upper* illustrates that the larger the contact length, the larger sliding friction force induces a faster droplet speed. The efficiency of gaining motility was estimated to be 67% based on the fraction of migrating droplets out of 63 droplets (*SI Appendix*, Fig. S5). All images were taken by epifluorescence microscopy. (Scale bars, 200 μm.)

ratio, suggesting that a longer L contributes to a larger total propulsive force (Fig. 5*G*).

Discussion

To summarize, actomyosin droplets offer a simple, but highly self-organized, system realizing both polarization of actomyosin networks and autonomous motion. The key is the physical interplay between the actin flow and membrane interface, indicating the unique dynamics of actomyosin networks that perform pattern formation and mechanical work. In previous studies, the cell-sized confinement was mainly used as a physical barrier to reconstitute the self-organization of intracellular actomyosin networks (16–21). Here, we resolved this bottleneck toward the realization of an active system that has the ability of membrane deformation and the increase of contractile forces using PIP_2 lipids in the membrane. Thus, the physical role of the membrane was expanded from a passive wall to an active interface generating a propulsive force. A previous study reported spontaneous random motion of undeformed droplets using microtubule–kinesin systems (34). Our actomyosin-based migratory droplets expanded such in vitro random motility into a directional one, providing an experimental model system of cell migration to explore key physical determinants of actomyosin-based motility.

In living cells, migration onset is triggered by the polarization of the actomyosin networks such that the actomyosin networks are accumulated at the one part of the membrane (35); thereafter, force transmission from the polarized actin flow to the substrate propels the cell body in confined environments, such as in tissues or microchannels (32, 36). Recent studies have shown that substrate friction tunes cell-migration speed (32). However, how such friction originates from the actin–membrane interaction has been unclear. In this study, by developing an in vitro migratory cell model, we revealed the physical features of actin–membrane interaction and the membrane–substrate interaction. Strikingly, our results showed that 1) actin–membrane binding and 2) substrate contact are sufficient to transmit contractile forces to the external environment, uncovering the essential physical determinants for efficient force transmission. Note that the localization of actin at the extracts/oil interface was not visible during the droplet migration, while the droplet deformation coupled with the propagation of actin waves suggests that there is a strong interaction between the actin filaments and lipids (Fig. 1*I* and Movies S2 and S3). These observations also indicate that the physical interaction of the dynamic actin flow with the membrane boundary is important to generate propulsive force. Indeed, our model only considers the local shear stress generated by actin flow interacting with the lipid boundary, which explained the actomyosin droplet migration under confinement.

In addition to the physical interaction between the actin flow and the lipid membrane imposed by PIP_2 lipids, we identified that only the physical interaction of either F-actin cross-linker α-actinin or an activator of the Arp2/3-mediated F-actin polymerization VVCA with the droplet interface also enabled droplet migration (*SI Appendix*, Fig. S2). Interestingly, the actin-flow speed with the membrane-bound α-actinin was faster than the case of membrane-bound VVCA, resulting in the faster migration speed with the membrane-bound α-actinin (*SI Appendix*, Fig. S3). A previous study using *Xenopus* egg extracts reported the faster actin-flow speed in the presence of α-actinin than ActA, which activates the Arp2/3 complex to nucleate branched F-actin (19). Our observation implies that the architecture of the network might contribute to the migration capacity by changing the contractile speed of the actomyosin network.

Moreover, we found that the migration speed of actomyosin droplets can be controlled through confinement geometry. This was explained by the active gel theory that the geometry-dependent balance between sliding friction force and fluid drag determines the migration speed. On the one hand, in 2D confinement, both friction force and fluid drag are altered for pancake-shaped droplets; thus, migration is damped under strong confinement. On the other hand, in 1D confinement, the elongated shape of the droplets could increase their friction force, enabling faster migration, even under strong confinement. Understanding such fundamental physical limitations in confined spaces allows us to set the founding ground to control actomyosin-based motility from in vitro models to in vivo situations.

It should be noted that our phenomenological geometric scaling is based on the experimental fact that the total transmitted contractile force is proportional to the contact area, which, thus, does not uniquely determine a microscopic model of the actomyosin-based motility. Substrate friction was also previously proposed to play an important role during bleb-based cell migration (37, 38). Nevertheless, the essence of the scaling theory remains unchanged if the strength of the contractile force is proportional to the area at which actin filaments are bound to the membrane. Detailed theoretical modeling beyond the geometric scaling remained as significant future work to classify actomyosin-based motility at the microscopic level.

Recent studies have shown that mechanical stress on the cell nucleus imposed by confinement triggers mechanochemical signaling pathways, and, in turn, contractility is enhanced in confined cells (9–11). This might be an adaptation strategy of living cells to migrate under strong confinement: Actomyosin droplet migration is overdamped by the viscous dissipation of the surrounding fluid, whereas the living cells could overcome this physical limitation by enhancing the contractility via mechanochemical signaling. Such adaptive responses to mechanical stimuli could further expand the migration capacity of confined actomyosin networks. To shed further light on the mechanical roles and self-organization principles of active gels obscured by a rich complexity of living organisms, the development of cell-mimetic active droplets that organize chemical–mechanical interplay would be a fruitful future challenge.

Materials and Methods

Preparation of *Xenopus* Egg Extracts. Actin-intact extracts were prepared from *X. laevis* unfertilized eggs according to a previously described method (20). Immediately after preparing the extracts, 1/1,000 volume of protease inhibitors (10 mg · mL^{-1} leupeptin, 10 mg · mL^{-1} pepstatin A, and 10 mg · mL^{-1} chymostatin dissolved in dimethyl sulfoxide [DMSO]), 1/20 volume of 2 M sucrose, and 1/20 volume of energy mix (150 mM creatine phosphate, 20 mM ATP, and 20 mM $MgCl_2$) were added. The extracts were then divided into 20-μL aliquots, snap-frozen in liquid nitrogen, and stored at −84 °C.

Protein Preparations. The VVCA domain of mouse N-WASP complementary DNA (384 to 501 aa) was cloned into the pCold-I vector (Takara), expressed in *Escherichia coli* [Rosetta(DE3), Merck Millipore] at 15 °C overnight in the presence of 1 mM isopropyl ß-D-1-thiogalactopyranoside (IPTG). The ×6 histidine-tagged mutant was purified on a Ni Sepharose 6 Fast Flow column (Cytiva), followed by dialysis against A50 buffer [50 mM Hepes–KOH, pH 7.6, 50 mM KCl, 5 mM $MgCl_2$, and 1 mM ethylene glycol-bis(β-aminoethyl ether)-*N*,*N*,*N*′,*N*′-tetraacetic acid (EGTA)] containing 1 mM dithiothreitol (DTT) at 4 °C. Recombinant human α-actinin I (×6 histidine-tagged) was prepared according to our previous study (39). Purified α-actinin was dialyzed overnight against A150 buffer (50 mM Hepes–KOH, pH 7.6, 150 mM KCl, 5 mM $MgCl_2$, and 1 mM EGTA) containing 1 mM 2-mercaptoethanol at 2 °C. Alexa Fluor 546-labeled actin was prepared by reacting the dye (Alexa Fluor 546 NHS Ester, Thermo) with actin in the filamentous

form purified from rabbit skeletal muscle in A50 buffer containing 1 mM DTT, then dialyzed against G-buffer (2 mM Tris·HCl, pH 8.0, 50 μM $CaCl_2$, 2 mM NaN_3, 0.1 mM ATP, and 0.5 mM 2-mercaptoethanol) to transform filaments into monomeric actin. The monomeric actin was further purified by using gel-filtration chromatography (Superdex 200 Increase 10/300 GL, Cytiva) and kept on ice until use. GFP-Lifeact (×6 histidine-tagged) cloned into pCold vector (Takara) was expressed in *E. coli* [BL21(DE3), New England Biolabs] at 15 °C overnight in the presence of 1 mM IPTG. The protein was purified on a Ni Sepharose 6 Fast Flow column (Cytiva), followed by digestion of the His-tag by Tobacco Etch Virus protease. The His-tag-removed GFP-Lifeact was further purified by using gel-filtration chromatography (Superdex 200 Increase 10/300 GL, Cytiva) and stored in A50 buffer containing 1 mM DTT.

Preparation of PDMS-Coated Glass slides. Glass slides were coated with a silicone elastomer (PDMS) (Sylgard 184; Dow Corning). Uncured PDMS mixed with a curing agent was poured onto the glass slides, and then PDMS was spread by using a spin-coater (1,000 rpm, 20 s). PDMS-coated glass slides were cured for 1 h at 75 °C. PDMS-coated coverslips (18 × 18 mm^2) were prepared by cutting the PDMS-coated glass with a glass cutter.

Encapsulation of Extracts in Droplets. Droplets were generated using a method described in a previous study (20). First, an aliquot of the extracts (20 μL) frozen in −84 °C was thawed and then incubated on ice for 1 h. Next, 0.2 μL of 100 μM TMR-Lifeact dissolved in DMSO (final 1 μM) and 0.2 μL of 10 mM nocodazole dissolved in DMSO (final 100 μM) were added to the extracts. At the same time, 0.2 μL of 3 mg · mL^{-1} purified GFP was added to the extracts when the contact area between the droplet and substrate was measured. Then, 0.4 μL of the extracts was injected into 20 μL of lipid–oil mixture (1 mM L-α-phosphatidyl choline from egg yolk (eggPC) (catalog no. 27554-01; Nacalai Tesque) in mineral oil (catalog no. M5904; Sigma-Aldrich) for control, and a mole fraction of 14% L-α-Phosphatidyl-D-myo-inositol-4,5-bisphosphate, Triammonium Salt, Porcine Brain (PIP_2) (catalog no. 524644; Merck) in 1 mM L-α-phosphatidyl choline from egg yolk in mineral oil for actin-membrane binding). The 1,2-di-(9Z-octadecenoyl)-*sn*-glycero-3-[(*N*-(5-amino-1-carboxypentyl)iminodiacetic acid)succinyl] (catalog no. 790404; Avanti Polar Lipids) was mixed with 1 mM eggPC in mineral oil with a mole fraction of 7.6% for experiments using 200 nM His–α-actinin and 10% for experiments using 10 nM His–VVCA (*SI Appendix*, Figs. S2 and S3 and Movie S4). Before injecting the extracts, the lipid–oil mixtures were incubated on ice for more than 5 min. The viscosity of M5904 $\eta_{oil} = 24.2$ mPa · s and low-viscosity oil of $\eta_{oil} = 14.8$ mPa · s prepared by mixing 200 μL of M5904 and 41 μL of hexadecane (catalog no. 080-03685; Nacalai Tesque) were measured by using an Ostwald viscometer (ϕ 0.75 mm) (catalog no. 2-8190-02; AS ONE) at 20 °C in a heat bath. By tapping the sample tube with a finger, we obtained a polydisperse emulsion of extracts-in-oil. Immediately after emulsification, 3 to 7 μL of the emulsion was placed on a PDMS-coated glass slide and gently covered with a PDMS-coated coverslip on top. The chamber height was controlled by the spacer thickness.

Magnetic Manipulation of Actomyosin Networks. First, 300 μL of magnetic beads (catalog no. S1420S, Streptavidin Magnetic Beads; BioLabs) (diameter = 1 μm, 4 mg · mL^{-1}) were added to a 1.5-mL tube, and the supernatants were removed while pulling the magnetic beads using a neodymium magnet. The remaining magnetic beads were washed with 300 μL of A50 buffer containing 1 mM DTT, and the supernatants were removed while pulling the magnetic beads using a neodymium magnet. The A50 buffer did not affect actomyosin activity (39). The washing process was repeated three times. After removing the supernatants, 50 μL of A50 buffer was added (final 24 mg · mL^{-1}). Before emulsification, 0.4 μL of the magnetic beads was added to the extracts, which was, in turn, accumulated by the contracted actomyosin gel. The position of the actomyosin gel entangled with magnetic beads was controlled by an external magnetic field by placing the neodymium magnet next to the observation chamber. For image acquisition to compare the migration speed of polarized actomyosin droplets with and without actin–membrane binding, polarization was initially built by a magnetic force in the actomyosin droplet. Thereafter, the magnet was removed, and time-lapse images were acquired. For image acquisition of the actomyosin droplet recovering the migration capacity by magnetic force-induced polarization, the magnet was kept next to the observation chamber. The chamber height was 100 μm for all the data.

Force-Transmission Microscopy. First, 2 μL of fluorescently labeled silica beads (silicastar-greenF, catalog no. 42–00-103; Corefront) (diameter = 3 μm, 50 mg · mL^{-1}) were mixed with 98 μL of MilliQ water. The solution was centrifuged at 15,000 rpm for 5 min. The supernatant was removed by pipette aspiration, and the residual bead suspension was dried to evaporate the residual MilliQ water on a heat block at 37 °C for 20 min. After completely drying the beads, 100 μL of mineral oil (catalog no. M5904; Sigma-Aldrich) was added to the beads, and the resulting 1 mg · mL^{-1} beads–oil mixture was sonicated for 20 min for resuspension. Next, a flow cell with a height of 100 μm was constructed by using PDMS-coated glass slides and noncoated coverslips. The chamber height was controlled by using a double-sided spacer tape. To place the beads on the bottom PDMS-coated glass surface, a 15-μL beads–oil mixture was injected into the flow cell. The flow cell was incubated for 30 min to allow sedimentation of the beads. After incubation, the top coverslips were gently removed. The excess amount of the beads–oil mixture was absorbed by a filter paper. Finally, actomyosin droplets were placed on the beads-covered PDMS-coated glass slides and gently sealed with a PDMS-coated coverslip on top. The chamber height was 100 μm for all the data.

Encapsulation of the Extracts in Annulus 1D Microchannel. Chromium masks (MITANI Micronics) were used to print patterns on SU-8 3025 photoresist (MicroChem) spin-coated on a silicon wafer using a mask aligner (MS-A100; MIKASA). The molds of the PDMS microwells were constructed on the surface of the silicon wafers. The PDMS elastomer was poured onto the mold and cured at 75 °C for 1 h. The patterned PDMS chamber was gently removed from the mold. The depth of the microwells was measured by using a laser-scanning surface profiler (LT-9000; Keyence). The chamber was stored in MilliQ water overnight in a fridge to hydrate. After placing 3 to 7 μL of the emulsion on a PDMS-coated glass slide, the PDMS chamber was gently placed on top of the emulsion droplets. We chose this quasi-1D geometry of the annulus microchannel because the straight 1D channel with inlet and outlet disturbed the initial polarization and induced unexpected drift flows.

Microscopy. Time-lapse images were acquired every 6 s by using an epifluorescence microscope (IX73; Olympus) equipped with a ×10 objective lens (U Plan WD 10×/0.25; Meiji Techno Japan) or a ×20 objective lens (TU Plan ELWD 20×/0.40; Nikon), a cooled complementary metal-oxide semiconductor camera (Neo5.5; Andor Technology), and a stable excitation light source (XLED1; Lumen Dynamics). The contact area between the droplet and substrate was recorded by using a confocal microscope (catalog no. IX73; Olympus) and a confocal scanning unit (CSU-X1; Yokogawa Electric Cor. Ltd.) equipped with an electron microscopy–charge-coupled device (EM-CCD) camera (iXon-Ultra; Andor Technologies) under a 488-nm fluorescence channel. For all microscopic examinations, the sample temperature was maintained at 20 ± 1 °C, using a custom-made heat block connected to a water-bath circulator and controlling the room temperature.

Image Analysis. Quantitative image analysis was performed by using a custom code written in MATLAB. The center of mass of each droplet was detected through the binarization of bright-field images. To determine the radius R and diameter $D = 2R$ of the droplets, the area of each droplet S was extracted and then calculated from $R = \sqrt{S/\pi}$. The aspect ratio of the droplet with $h > D$ was set to $h/D = 1$. The droplet speed V_{drop} was calculated from the straight displacement of the droplet centroid from the initial position to the final position divided by the track duration. The migration speed of the droplets under 2D confinement was calculated from the displacement within 10 min. The migration speed of the droplets under the 1D microchannel was calculated from the displacement within 5 min. The contact angle used for the calculation of $f(\theta)$ was estimated from the droplets confined under 1D annulus microchannels by linear fitting of the binarized image at the contact point (*SI Appendix*, Fig. S13). Quantification of the speed of actin flow was performed by producing kymographs of the fluorescence images. To extract the position of the beads in force-transmission microscopy, particle-tracking analysis was performed by using the Fiji plugin TrackMate (40).

FRAP. FRAP experiments were performed on an epifluorescence microscope (IX73; Olympus) equipped with the EM-CCD camera using a laser light (Cobolt, 532 nm, 25 mW). Bleaching was done on a circular region with

the Gaussian radius of ∼20 μm in the vicinity of a lateral droplet surface where membrane-bound actin network exists in the presence of PIP_2 (total bleach time 10 s). The actin network was visualized by adding GFP-Lifeact (1.0 μM, to observe the localization) and Alexa Fluor 546-labeled G-actin (0.4 μM, 100% labeled, to observe the actin dynamics) into extracts instead of TMR-Lifeact prior to droplet formation. Imaging of the area was resumed immediately after photobleaching and continued every 1 s for 3 min. All the postbleach values were divided by the values of the last time point. The first postbleach measurement was set to 0 s. The analysis of the FRAP recovery data was performed by using a custom code written in MATLAB.

Statistical analysis. Statistical analysis was carried out by using MATLAB. The *P* values were determined by Mann–Whitney *u* test.

Data Availability. All study data are included in the article and/or *SI Appendix*.

ACKNOWLEDGMENTS. We thank T. Q. P. Ueda and Y. Okada for sharing materials and J. Ikenouchi for fruitful discussion. This work was supported by Scientific Research (B) Grants 20H01872 (to Y.T.M.) and 19H03201 (to Y.S.); Scientific Research on Innovative Areas "Molecular Engines" Grants 18H05427 (to Y.T.M.) and 19H05393 (to M.M.); Japan Society for the Promotion of Science Fellows Grant JP19J20035 (to R.S.); Challenging Research (Exploratory) Grants 21K18605 (to Y.T.M.) and 20K21404 (to Y.S.) from the Ministry of Education, Culture, Sports, Science, and Technology, Japan; Human Frontier Science Program Research Grant RGP0037/2015 (to Y.T.M.); The Hakubi Project of Kyoto University (M.M.); and Japan Science and Technology Agency PRESTO, Japan Grant JPMJPR20ED (to M.M.).

Author affiliations: [a]Department of Physics, Graduate School of Science, Kyushu University, Fukuoka 819-0395, Japan; [b]School of Physics and Astronomy, University of Minnesota, Minneapolis, MN 55455; [c]Department of Chromosome Science, National Institute of Genetics, Mishima 411-8540, Japan; [d]Hakubi Center for Advanced Research, Kyoto University, Kyoto 606-8501, Japan; [e]Department of Physics, Graduate School of Science, Kyoto University, Kyoto 606-8502, Japan; [f]Institut Curie, Paris Sciences et Lettres Research University, UMR 144, CNRS, F-75005 Paris, France; and [g]PRESTO, Japan Science and Technology Agency, Kawaguchi 332-0012, Japan

1. J. Sedzinski *et al.*, Polar actomyosin contractility destabilizes the position of the cytokinetic furrow. *Nature* **476**, 462–466 (2011).
2. Y.-J. Liu *et al.*, Confinement and low adhesion induce fast amoeboid migration of slow mesenchymal cells. *Cell* **160**, 659–672 (2015).
3. A. Reversat *et al.*, Cellular locomotion using environmental topography. *Nature* **582**, 582–585 (2020).
4. S. Shamipour *et al.*, Bulk actin dynamics drive phase segregation in zebrafish oocytes. *Cell* **177**, 1463–1479.e18 (2019).
5. J. Prost, F. Jülicher, J.-F. Joanny, Active gel physics. *Nat. Phys.* **11**, 111–117 (2015).
6. D. L. Bodor, W. Pönisch, R. G. Endres, E. K. Paluch, Of cell shapes and motion: The physical basis of animal cell migration. *Dev. Cell* **52**, 550–562 (2020).
7. K. M. Yamada, M. Sixt, Mechanisms of 3D cell migration. *Nat. Rev. Mol. Cell Biol.* **20**, 738–752 (2019).
8. E. K. Paluch, I. M. Aspalter, M. Sixt, Focal adhesion-independent cell migration. *Annu. Rev. Cell Dev. Biol.* **32**, 469–490 (2016).
9. V. Venturini *et al.*, The nucleus measures shape changes for cellular proprioception to control dynamic cell behavior. *Science* **370**, eaba2644 (2020).
10. A. Elosegui-Artola *et al.*, Force triggers YAP nuclear entry by regulating transport across nuclear pores. *Cell* **171**, 1397–1410.e14 (2017).
11. C. Rianna, M. Radmacher, S. Kumar, Direct evidence that tumor cells soften when navigating confined spaces. *Mol. Biol. Cell* **31**, 1726–1734 (2020).
12. C. M. Field *et al.*, Actin behavior in bulk cytoplasm is cell cycle regulated in early vertebrate embryos. *J. Cell Sci.* **124**, 2086–2095 (2011).
13. S. Köhler, A. R. Bausch, Contraction mechanisms in composite active actin networks. *PLoS One* **7**, e39869 (2012).
14. A.-C. Reymann *et al.*, Actin network architecture can determine myosin motor activity. *Science* **336**, 1310–1314 (2012).
15. M. Murrell *et al.*, Spreading dynamics of biomimetic actin cortices. *Biophys. J.* **100**, 1400–1409 (2011).
16. E. Abu-Shah, K. Keren, Symmetry breaking in reconstituted actin cortices. *eLife* **3**, e01433 (2014).
17. T. H. Tan *et al.*, Self-organized stress patterns drive state transitions in actin cortices. *Sci. Adv.* **4**, eaar2847 (2018).
18. M. Pinot *et al.*, Confinement induces actin flow in a meiotic cytoplasm. *Proc. Natl. Acad. Sci. U.S.A.* **109**, 11705–11710 (2012).
19. M. Malik-Garbi *et al.*, Scaling behaviour in steady-state contracting actomyosin networks. *Nat. Phys.* **15**, 509–516 (2019).
20. R. Sakamoto *et al.*, Tug-of-war between actomyosin-driven antagonistic forces determines the positioning symmetry in cell-sized confinement. *Nat. Commun.* **11**, 3063 (2020).
21. N. Ierushalmi *et al.*, Centering and symmetry breaking in confined contracting actomyosin networks. *eLife* **9**, e55368 (2020).
22. J. Riedl *et al.*, Lifeact: A versatile marker to visualize F-actin. *Nat. Methods* **5**, 605–607 (2008).
23. K. Fukami, T. Endo, M. Imamura, T. Takenawa, α-Actinin and vinculin are PIP_2-binding proteins involved in signaling by tyrosine kinase. *J. Biol. Chem.* **269**, 1518–1522 (1994).
24. C. F. Kelley *et al.*, Phosphoinositides regulate force-independent interactions between talin, vinculin, and actin. *eLife* **9**, e56110 (2020).
25. J. Saarikangas, H. Zhao, P. Lappalainen, Regulation of the actin cytoskeleton-plasma membrane interplay by phosphoinositides. *Physiol. Rev.* **90**, 259–289 (2010).
26. R. Rohatgi, H. Y. Ho, M. W. Kirschner, Mechanism of N-WASP activation by CDC42 and phosphatidylinositol 4, 5-bisphosphate. *J. Cell Biol.* **150**, 1299–1310 (2000).
27. H. N. Higgs, T. D. Pollard, Activation by Cdc42 and PIP(2) of Wiskott-Aldrich syndrome protein (WASp) stimulates actin nucleation by Arp2/3 complex. *J. Cell Biol.* **150**, 1311–1320 (2000).
28. A. M. Lebensohn, L. Ma, H.-Y. H. Ho, M. W. Kirschner, Cdc42 and PI(4,5)P2-induced actin assembly in *Xenopus* egg extracts. *Methods Enzymol.* **406**, 156–173 (2006).
29. B. A. Smith *et al.*, Three-color single molecule imaging shows WASP detachment from Arp2/3 complex triggers actin filament branch formation. *eLife* **2**, e01008 (2013).
30. M. Abercrombie, J. E. Heaysman, S. M. Pegrum, The locomotion of fibroblasts in culture. 3. Movements of particles on the dorsal surface of the leading lamella. *Exp. Cell Res.* **62**, 389–398 (1970).
31. A. R. Bausch, F. Ziemann, A. A. Boulbitch, K. Jacobson, E. Sackmann, Local measurements of viscoelastic parameters of adherent cell surfaces by magnetic bead microrheometry. *Biophys. J.* **75**, 2038–2049 (1998).
32. M. Bergert *et al.*, Force transmission during adhesion-independent migration. *Nat. Cell Biol.* **17**, 524–529 (2015).
33. A. Eri, K. Okumura, Viscous drag friction acting on a fluid drop confined in between two plates. *Soft Matter* **7**, 5648–5653 (2011).
34. T. Sanchez, D. T. N. Chen, S. J. DeCamp, M. Heymann, Z. Dogic, Spontaneous motion in hierarchically assembled active matter. *Nature* **491**, 431–434 (2012).
35. V. Ruprecht *et al.*, Cortical contractility triggers a stochastic switch to fast amoeboid cell motility. *Cell* **160**, 673–685 (2015).
36. L. Aoun *et al.*, Leukocyte transmigration and longitudinal forward-thrusting force in a microfluidic Transwell device. *Biophys. J.* **120**, 2205–2221 (2021).
37. B. Maugis *et al.*, Dynamic instability of the intracellular pressure drives bleb-based motility. *J. Cell Sci.* **123**, 3884–3892 (2010).
38. G. Charras, E. Paluch, Blebs lead the way: How to migrate without lamellipodia. *Nat. Rev. Mol. Cell Biol.* **9**, 730–736 (2008).
39. M. Miyazaki, M. Chiba, H. Eguchi, T. Ohki, S. Ishiwata, Cell-sized spherical confinement induces the spontaneous formation of contractile actomyosin rings *in vitro*. *Nat. Cell Biol.* **17**, 480–489 (2015).
40. J.-Y. Tinevez *et al.*, TrackMate: An open and extensible platform for single-particle tracking. *Methods* **115**, 80–90 (2017).